BIOCHEMISTRY
including biophysical chemistry & molecular biology

Article

pubs.acs.org/biochemistry

Active Site Loop Dynamics of a Class IIa Fructose 1,6-Bisphosphate Aldolase from *Mycobacterium tuberculosis*

Scott D. Pegan,*[,†] Kamolchanok Rukseree,[‡,§] Glenn C. Capodagli,[†] Erica A. Baker,[†] Olga Krasnykh,[§,∥] Scott G. Franzblau,[§,∥] and Andrew D. Mesecar*[,⊥]

[†]Eleanor Roosevelt Institute and Department of Chemistry and Biochemistry, University of Denver, Denver, Colorado 80208, United States

[‡]National Center for Genetic Engineering and Biotechnology (BIOTEC), NSTDA, Thailand Science Park, Tha Khlong 12120, Thailand

[§]Institute for Tuberculosis Research, University of Illinois at Chicago, Chicago, Illinois 60612, United States

[∥]Department of Medicinal Chemistry, University of Illinois at Chicago, Chicago, Illinois 60607, United States

[⊥]Departments of Biological Sciences and Chemistry and Purdue Center for Cancer Research, Purdue University, West Lafayette, Indiana 47907, United States

Supporting Information

ABSTRACT: Class II fructose 1,6-bisphosphate aldolases (FBAs, EC 4.1.2.13) comprise one of two families of aldolases. Instead of forming a Schiff base intermediate using an ϵ-amino group of a lysine side chain, class II FBAs utilize Zn(II) to stabilize a proposed hydroxyenolate intermediate (HEI) in the reversible cleavage of fructose 1,6-bisphosphate, forming glyceraldehyde 3-phosphate and dihydroxyacetone phosphate (DHAP). As class II FBAs have been shown to be essential in pathogenic bacteria, focus has been placed on these enzymes as potential antibacterial targets. Although structural studies of class II FBAs from *Mycobacterium tuberculosis* (MtFBA), other bacteria, and protozoa have been reported, the structure of the active site loop responsible for catalyzing the protonation−deprotonation steps of the reaction for class II FBAs has not yet been observed. We therefore utilized the potent class II FBA inhibitor phosphoglycolohydroxamate (PGH) as a mimic of the HEI- and DHAP-bound form of the enzyme and determined the X-ray structure of the MtFBA−PGH complex to 1.58 Å. Remarkably, we are able to observe well-defined electron density for the previously elusive active site loop of MtFBA trapped in a catalytically competent orientation. Utilization of this structural information and site-directed mutagenesis and kinetic studies conducted on a series of residues within the active site loop revealed that E169 facilitates a water-mediated deprotonation−protonation step of the MtFBA reaction mechanism. Also, solvent isotope effects on MtFBA and catalytically relevant mutants were used to probe the effect of loop flexibility on catalytic efficiency. Additionally, we also reveal the structure of MtFBA in its holoenzyme form.

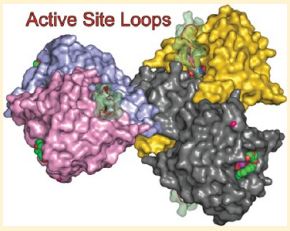

Class II fructose 1,6-bisphosphate aldolase (FBA, EC 4.1.2.13) catalyzes the second reversible step of the glycolytic pathway in the majority of protozoa, bacteria, fungi, and blue-green algae.[1] In doing so, FBA generates glyceraldehyde 3-phosphate (G3P) and dihydroxyacetone phosphate (DHAP) from the cleavage of the open chain form of fructose 1,6-bisphosphate [FBP (Figure 1)]. With DHAP rapidly converted to an additional G3P molecule by triosephosphate isomerase (EC 5.3.1.1), FBAs are critical for supplying downstream metabolic enzymes with G3P. In the reversible reaction when gluconeogensis is required, class II FBAs perform an adol condensation of DHAP and G3P to produce FBP (Figure 1).[2] Together, the substrates and products that these class II FBAs supply are crucial for any an organism's survival.

Class II FBAs comprise one of two families of aldolases. Both class II FBA and class I FBAs are proposed to have evolved independently from a common ancestor as they are all comprised of similar α/β folds.[3,4] Despite their common structural folds and tendencies to form dimeric or higher-order quaternary structures, class I and class II FBAs are strikingly different. Whereas class I FBAs utilize the ϵ-amino group of a lysine side chain to form a Schiff base intermediate during the reaction mechanism, class II FBAs require metal cations for catalysis, including an active site Zn(II) that stabilizes a putative hydroxyenolate intermediate (HEI). Additionally, class II FBAs are activated by monovalent cations, whereas class I FBAs have no such activation.[1,3,5]

In addition to differing in reaction mechanism, class I and II FBAs also differ in their distribution across species. Mammals rely on class I FBA for metabolism, while class II FBAs are present in only protozoa, bacteria, fungi, and blue-green algae. This distribution has prompted several investigations of whether class II FBAs are essential for microbial survival, particularly in bacteria that possess both class I and class II FBAs. In support of this assertion, FBA gene, *fbaB* (class I)

Received: July 11, 2012
Revised: January 3, 2013
Published: January 8, 2013

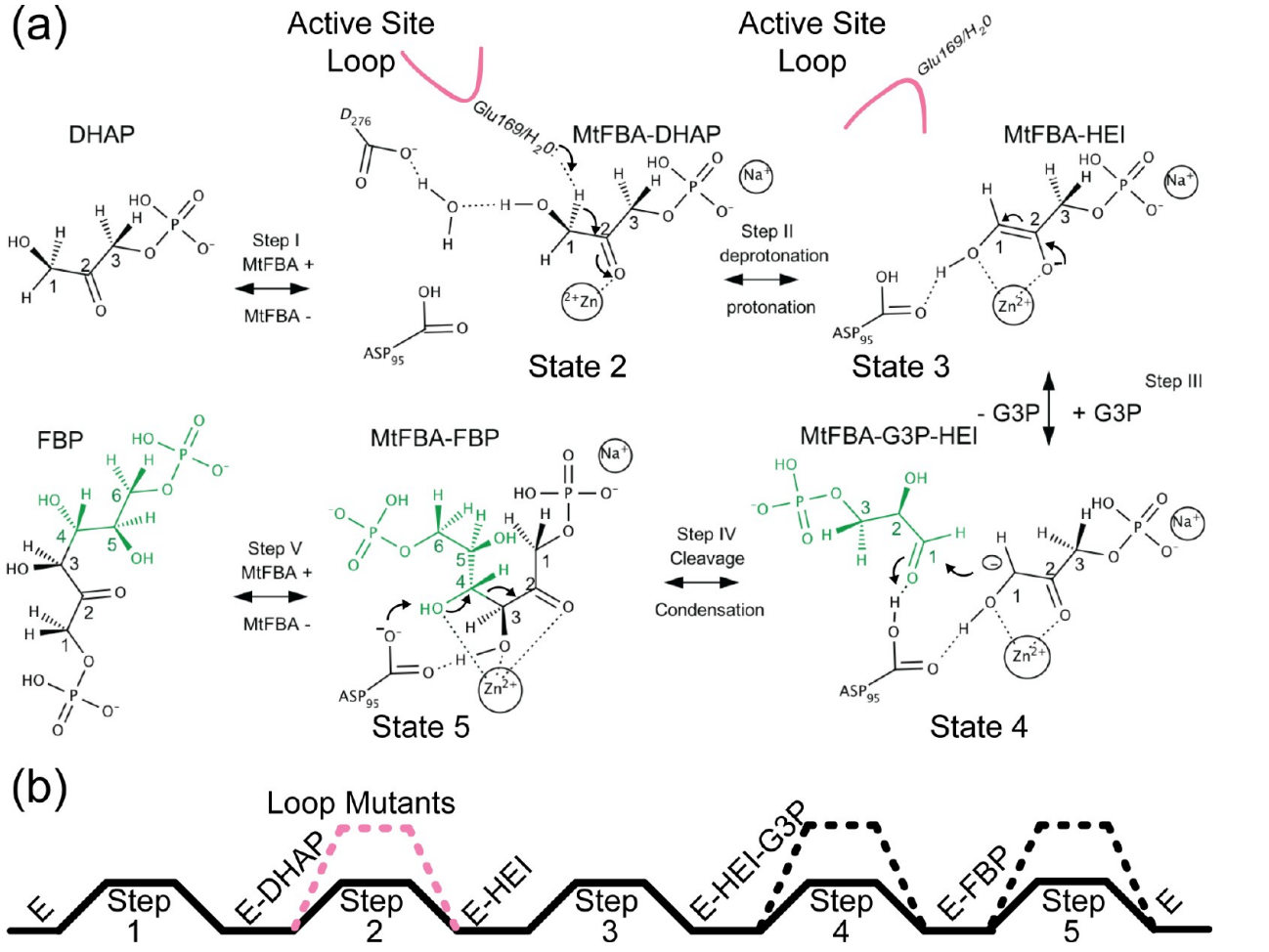

Figure 1. Proposed mechanism and reaction coordinate of MtFBA. (a) A five-step, reversible chemical mechanism of MtFBA is shown along with associated structural motion of the active site loop. Atoms of FBP, which originated from G3P, are colored green for the sake of clarity, and a pink line denotes the active site loop amino acids (168−179) of MtFBA. (b) Simplified reaction coordinate diagram for the MtFBA-catalyzed reaction illustrating intermediate and transition states. The dashed lines represent reaction steps that involve proton transfer steps where possible increases in the energy of the reaction barriers could occur because of these steps being sensitive to deuterium substitution.

knockout strains derived from bacteria autotrophic for both genes have been successfully obtained.[6,7] However, attempts to knock out the *fbaA* gene (class II) in *Mycobacterium tuberculosis*, *Escherichia coli*, and *Streptomyces galbus*, all of which contain both classes of FBA, resulted in nonviable bacteria.[2,6,8,9] Also, only significant bacterial expression levels of class I FBAs have been observed in the presence of gluconeogenic substrates or high-aeration conditions.[10,11] These results, along with upregulation of the class II FBA gene in *M. tuberculosis* under hypoxic conditions, suggest that class II FBAs are essential for bacterial survival.[12]

One of the prokaryotic class II FBAs that has been of recent focus is that from *M. tuberculosis*, the causative agent of tuberculosis.[2,13] Tuberculosis is one of the leading causes of mortality in developing countries, and one-third of the world's population is thought to harbor the bacterium.[14] With the emergence of the so-called "extensively" drug-resistant strains of *M. tuberculosis*, a new urgency exists for the development of novel therapeutics, and the class II FBA from *M. tuberculosis* (MtFBA) may serve as a new target.[15] MtFBA belongs to one of two class II subfamilies designated as class IIa. Members of each subfamily share 40% sequence homology compared to 25−30% across all class II FBAs.

We previously determined the high-resolution X-ray structures of MtFBA bound with DHAP, DHAP-G3P, and FBP, and these structures provided unique insight into the interactions of MtFBA with its substrates and into the reaction mechanism of this enzyme at the atomic level.[2] In addition, these structures also allowed us to visualize the putative hydroxyenolate intermediate (HEI) of the reaction, which was also the theoretical basis for the design of the first potent inhibitor of class II FBAs, phosphoglycolohydroxamate (PGH).[16] PGH has been shown to be a potent inhibitor of class II FBAs with measured K_i values of 37, 11, and 20−50 nM for class II FBAs from *Giardia lamblia*, *Saccharomyces cerevisiae*, and *E. coli* respectively.[16−18] Although we have reported the X-ray structures of MtFBA with its substrates and products, and the X-ray structures of the class IIa FBA enzyme from *E. coli* (EcFBA) and the class IIb FBAs from *G. lamblia* (GlFBA), *Thermus aquaticus* (TaFBA), and *Helicobacter pylori* (HpFBA) are also known, the structural and thermodynamic basis for the potency of PGH has yet to be fully determined.[2,13,19−21] This is in large part because all of the previously reported structures of class II FBAs are missing electron density for a catalytically important loop that contains an essential glutamate residue that is proposed to be directly involved in the protonation−

dx.doi.org/10.1021/bi300928u | *Biochemistry* 2013, 52, 912−925

deprotonation step of the MtFBA-mediated reaction (Figure 1).[22]

Because PGH is proposed to mimic the DHAP−HEI intermediate step of the FBA reaction where an amino acid residue would be required to act, either directly or indirectly through a water molecule, to deprotonate or protonate (step II, Figure 1), we determined the X-ray structure of PGH bound to MtFBA in an attempt to trap the active site loop in a catalytically relevant conformation. We also determined the X-ray structure of the zinc-bound, substrate-free form of MtFBA that proves that this catalytically required divalent metal cation is capable of binding to the free enzyme in contrast to another report.[9] On the basis of these structures, and those of MtFBA in complex with DHAP, DHAP-G3P, and FBP that we previously determined, we performed site-directed mutagenesis and kinetic studies to identify and more fully elucidate the roles of this catalytically relevant glutamate residue with respect to its interaction with PGH. Interestingly, this interaction occurs through a coordinated water molecule via a shuttle mechanism, likely mimicking its orientation during the protonation−deprotonation step of the MtFBA reaction mechanism. Finally, we probed the importance of several residues within the active site loop in the catalytic efficiency of MtFBA.

EXPERIMENTAL PROCEDURES

Materials. Chemicals, biochemicals, buffers, and solvents were purchased from Sigma-Aldrich Chemical Co. (St. Louis, MO), Fisher Scientific Inc. (Pittsburgh, PA), Fluka Chemical Corp. (Milwaukee, WI), or EM Science (Cincinnati, OH). Specifically for enzymatic assays, β-nicotinamide adenine dinucleotide, reduced dipotassium salt [NADH (Sigma catalog no. N4505)], nicotinamide adenine dinucleotide hydrate [NAD^+ (Sigma catalog no. 43407)], α-glycerophosphate dehydrogenase (Sigma catalog no. G6880), rabbit muscle triosephosphate isomerase [TIM (Sigma catalog no. T6258)], rabbit glyceraldehyde 3-phosphate dehydrogenase [GAPDH (Sigma catalog no. G2267)], D-fructose 1,6-bisphosphate tetra(cyclohexylammonium) salt [FBP (Sigma catalog no. F0752)], and dihydroxyacetone phosphate dilithium salt [DHAP (Sigma catalog no. D7137)] were used. The Vivaspin centrifugal filter devices were obtained from GE Healthcare (Piscataway, NJ). The Ni-NTA and the Superdex-S200 High Resolution resins were obtained from Qiagen (Valencia, CA) and GE Healthcare, respectively. Enzymes and reagents used for molecular biology procedures were obtained from Fermentas, Inc. (Glen Burnie, MD), Qiagen, and Agilent Technologies (Santa Clara, CA).

Synthesis of Phosphoglycolohydroxamate. Phosphoglycolamide (PGA), a precursor of PGH, and PGH itself were prepared from glycolamide according to a published procedure that uses available and inexpensive reagents, with minor modifications.[23] The first step (phosphorylation of glycolamide by polyphosphoric acid) was conducted at 44−48 °C. The reaction mixture was cooled; water and ice were added to the reaction mixture under vigorous stirring conditions to prevent pH fluctuations, which can lead to decomposition. Solid $Ba(OH)_2$ and $BaCO_3$ were then added in small portions until a pH of ∼8 was achieved. The resulting precipitate was filtered off, with the filtrate subsequently being concentrated under reduced pressure. After cooling at 4 °C, the resulting crystals of barium salt of PGA (first portion) were filtered out, washed with a cold mixture of ethanol and water, and then dried in the vacuum desiccator over P_2O_5. The inorganic barium salt precipitates were washed with a small amount of cold water and filtered. The resulting aqueous solution was concentrated, providing a second portion of barium salt of PGA, which was treated like the first. A Dowex 50x4 (H^+) (exchange capacity of 1.2 mequiv/mL) was used to obtain PGA from its barium salt (approximately 2 equiv of resin/equiv of salt).

For PGH synthesis, the water solution of PGA (after resin was filtered off) was treated with 15 equiv of hydroxylamine [50% (w/v) solution in water], with the reaction mixture kept overnight at room temperature, evaporated under vacuum, dried additionally under high vacuum, and used for preparing PGH−CHA salt without additional purification. The PGH was dissolved in water (approximately 30 mg/mL), and 6 equiv of cyclohexylamine was added under stirring, evaporated under vacuum, and then recrystallized from ethanol. Cyclohexylamine was preferred to the barium salt to prevent barium contamination of the MtFBA active site. To ensure the quality of the resulting PGH−CHA salt, ^{1}H NMR spectra were recorded at 400 MHz on a Bruker DPX-400 spectrometer for a 28 mg/mL solution in D_2O: ^{1}H NMR δ 0.95−1.30 (m, 10H), 1.44−1.94 (m, 10H), 3.02 (m, 2H, all cyclohexyl), 4.18 (d, J = 7 Hz, 2H, CH_2), 4.69 (H_2O); ^{13}C NMR δ 23.35, 23.84, 29.89, 49.87 (cyclohexyl), 62.02, 62.87 (CH_2), 169.30, 162.22 (C═O); ^{31}P NMR δ 3.55.

MtFBA Expression Vector and Site-Directed Mutagenesis of the *fba* Gene. The construction of the *M. tuberculosis* pET17b-*fba*H expression vector harboring the *fba* gene (Rv0363c) was previously described.[2] The expression system produces a C-terminal, His-tagged fusion protein, which is herein termed MtFBA. The residual His tag has been observed not to affect the overall structure of MtFBA or its in vitro activity.[2,9,24] Mutations in MtFBA were incorporated via the Quick-Change site-directed mutagenesis system (Agilent Technologies). The following oligonucleotides were used for mutagenesis with the altered bases in bold: 5′-CGGCGTCG-TCG**CC**G**CC**GAAGAGGACG-3′ (G166A/G167A), 5′-CGG-CGTCGTCGGCG**CC**GAAGAGGACG-3′ (G167A), 5′-CGT-CGGCGGCG**CA**GAGGACGGCG-3′ (E168A), and 5′-CGG-CGGCGAAG**C**GGACGGCGTGG-3′ (E169A). The resulting pET-fbaH mutant plasmids were introduced into *E. coli* XL-1 blue cells by heat-shock transformation and were then propagated and purified on a large scale for sequence verification and transformation into *E. coli* BL21(DE3) for enzyme expression. The complete coding regions for all mutant enzymes were sequenced using either the RRC DNA sequencing facility at the University of Illinois at Chicago or CU Cancer Center DNA Sequencing & Analysis Service.

Production and Purification of Wild-Type and Mutant MtFBA. *E. coli* BL21(DE3) cells harboring either wild-type or mutant pET-*fba*H were grown at 37 °C in 8 L (8 × 1 L) of LB broth containing 100 μg/mL ampicillin until the OD_{600} was approximately 0.6. Expression of the *fba*H gene was induced by the addition of IPTG to a final concentration of 0.4 mM, and the culture was allowed to grow for an additional 4−6 h at 25 °C. After this time period, bacterial cells were harvested by centrifugation at 3000*g* for 15 min. Cells were washed with PBS and stored at −20 °C until they were used. The cell pellets collected from the 8 L culture were suspended in buffer A [50 mM sodium phosphate buffer (pH 8.0) and 300 mM NaCl] and subsequently lysed by the addition of 5 mg of chicken lysozyme followed by sonication using a Gex 600 Ultrasonic Processor (Footswitch). Sonication pulse settings were 5 s on and 5 s off for a total on time of 5 min at 60% amplitude.

Insoluble cell debris was removed by centrifugation at 16000*g* for 45 min at 4 °C. MtFBA was purified from the soluble fraction by nickel affinity and size exclusion according to our previously described methods.[2] The resulting purified wild-type and mutant MtFBA enzymes were exchanged into buffer B [20 mM Tricine buffer (pH 8), 100 mM NaCl, 0.1 mM $ZnCl_2$, and 2 mM DTT] and then concentrated to 15 mg/mL using ultrafiltration units fitted with 10000 molecular weight cutoff filters (GE Healthcare). The final protein was also filtered through 0.65 μm membrane filters to remove any precipitate. After purification, the concentrations of all proteins were determined by the absorbance at 280 nm using molar extinction coefficients experimentally derived by the method of Gill and von Hippel, 23044 M^{-1} cm^{-1} or 0.619 L g^{-1} cm^{-1}.[25]

Isothermal Titration Calorimetry (ITC) Experiments. ITC experiments were conducted using a VP-ITC system (Microcal, Amherst, MA). Degassed protein samples for wild-type and G166A/G167A MtFBA were used, and titrations were performed at 25.2 °C. Prior to being degassed, both proteins were dialyzed against a solution of 50 mM Tricine (pH 7.5), 100 mM NaCl, 0.1 mM $ZnCl_2$, and 2 mM DTT. Isothermal titrations of wild-type MtFBA with PGH were performed in duplicate and were comprised of 60 (1.5 μL) injections of 2 mM PGH into 80 μM wild-type MtFBA. Isothermal titrations of wild-type MtFBA with DHAP were performed using the same experimental parameters that were used with PGH except that PGH was substituted for 2 mM DHAP. Time delays between injections were set at 300 s for the initial delay and then 200 s between subsequent injections. Isothermal titrations of G166A/G167A MtFBA with PGH were performed with 60 μM protein and with delay times between injections of 500 s. All other parameters remained the same as those with wild-type MFBA. The average heat released (kilocalories per mole of injectant) of the last five injections was used to correct for the heat of dilution. All ITC data sets were analyzed and fit to a single-site binding model using nonlinear curve fitting procedures in ORIGIN 5.0 (MicroCal Systems).

MtFBA Enzymatic FBP Cleavage Assays. The coupled assay for the FBP cleavage activity of FBA was conducted as described previously with slight modifications.[4] The assay mixture (final volume of 100 μL) contained 0.4 mM NADH, 2 units/mL rabbit muscle α-glycerophosphate dehydrogenase, 20 units/mL rabbit muscle TIM, 0.02% (w/v) BSA, 100 mM potassium acetate, 100 mM Tris-HCl (pH 7.8), and wild-type (0.134 μM) and mutant MtFBAs (0.537 μM for E168A, 161 μM for E169A, 10.7 μM for G167A, 10.7 μM for G166A/G167A, and 0.269 μM for D276A). The reaction was initiated by the addition of FBP (final concentration ranging from 0 to 2000 μM). All assays were performed at room temperature and in triplicate using 96-well, flat-bottom polystyrene plates (Fisherbrand). All MtFBA activity assays were conducted using a Molecular Devices SpectraMax384 Plus plate reader by measuring the decrease in NADH absorbance at 340 nm (ε = 6220 M^{-1} cm^{-1}). The path length for the assay was determined to be 0.36 cm. To determine the kinetic parameters V_{max} and K_m, rates derived from initial velocity data were fit to the Michaelis–Menten equation, $v = V_{max}/(1 + K_m/[S])$, using Enzyme Kinetics Module version 1.3 of Sigma Plot version 10 (SPSS Inc.). Values for k_{cat} were calculated from V_{max} using the total enzyme concentration [E] via the equation $k_{cat} = V_{max}/[E]$. One unit of aldolase activity is defined as the amount of enzyme that catalyzes the cleavage of 1 μmol of FBP/min under the conditions of the assay. All turnover number (k_{cat}) values were calculated using the concentration of a monomer of MtFBA.

Solvent Isotope Effects. To evaluate the solvent (D_2O) kinetic solvent isotope effects on the MtFBA reaction, enzyme activity measurements were performed in a reaction mixture containing >94.5% D_2O. This was achieved by bringing up all of the assay reagents in 99.9% D_2O (Sigma catalog no. 364312). To minimize the amount of H^+ in solution, all reagent solutions were generated from anhydrous salts, or lyophilized enzymes, just prior to the assay to ensure a minimal exchange of water with air. Additionally, wild-type and mutant MtFBAs were diluted to their working stock concentrations in D_2O. This minimized the only source of H_2O to negligible carryover from the purification of MtFBAs themselves and the 10 μL of the buffer that was used, which comprises only 5.5% of the assay volume. The relation of pH to pD was determined using the equation pH = pD + 0.4.[26] The activity of MtFBA at the resulting pD value, 7.4, is predicted to fall within approximately 15% of that at its optimal pH, 7.8.[4]

Determination of the IC_{50} of PGH. The affinity of PGH for MtFBA was estimated by determining the IC_{50} value for the interaction. The experimental conditions used were the same as those for determining the K_m values for FBP with the exception that PGH concentrations were varied from 0 to 20 μM at a fixed FBP concentration of 40 μM (the K_m value for FBP). To determine the IC_{50} value for PGH, the percent inhibition (I%) was calculated using the formula $I\% = [1 - (v_{sample} - v_{negative\ control})/(v_{positive\ control} - v_{negative\ control})] \times 100$. The resulting I% values were plotted as a function of PGH concentration, and the data were fit via nonlinear regression to the equation $I\% = I\%_{max}/(1 + IC_{50}/[PGH])$.

Determination of the K_i of DHAP. For determination of the K_i value for DHAP, we had to modify the MtFBA enzymatic cleavage assay to prevent degradation of DHAP.[21] To achieve this, rabbit muscle α-glycerophosphate dehydrogenase was replaced with rabbit GAPDH to couple MtFBA-produced G3P to the reduction of NAD^+. Thus, MtFBA activity was observed through an increase in absorbance at 340 nm. Furthermore, TIM was removed and potassium arsenate added to mimic phosphate as a GAPDH cosubstrate. The final assay mixture contained 0.2 mM NAD^+, 5 units/mL rabbit GAPDH, 0.02% (w/v) BSA, 100 mM potassium acetate, 5 mM potassium arsenate, 100 mM Tris-HCl (pH 7.8), and 0.002 mg/mL wild-type MtFBA. MtFBA inhibition studies with DHAP as the varied substrate were conducted using five DHAP concentrations, from 0 to 4000 μM, and four FBP concentrations from 8 to 80 μM. Initial velocity data were fit, using nonlinear regression analysis, to each of the equations describing partial and full models of competitive, uncompetitive, noncompetitive, and mixed inhibition using the Enzyme Kinetics Module version 1.3 of Sigma Plot (version 10, SPSS Inc.). On the basis of the analysis of fits through "goodness-of-fit" statistics, the full competitive inhibition model with the equation $v = V_{max}/[1 + (K_m/[S])(1 + [I]/K_i)]$ was found to fit the kinetic inhibition data best, where [S] = [DHAP], [I] = [FBP], and K_i is the constant for dissociation of FPB from free MtFBA.

MtFBA and MtFBA–PGH Crystallization. Initial cocrystallization conditions for the MtFBA–PGH complex were achieved using conditions from our previously described crystallization protocols.[2] Final cocrystals of the MtFBA–PGH complex structure were grown using hanging-drop vapor diffusion at room temperature. Crystallization drops included 4

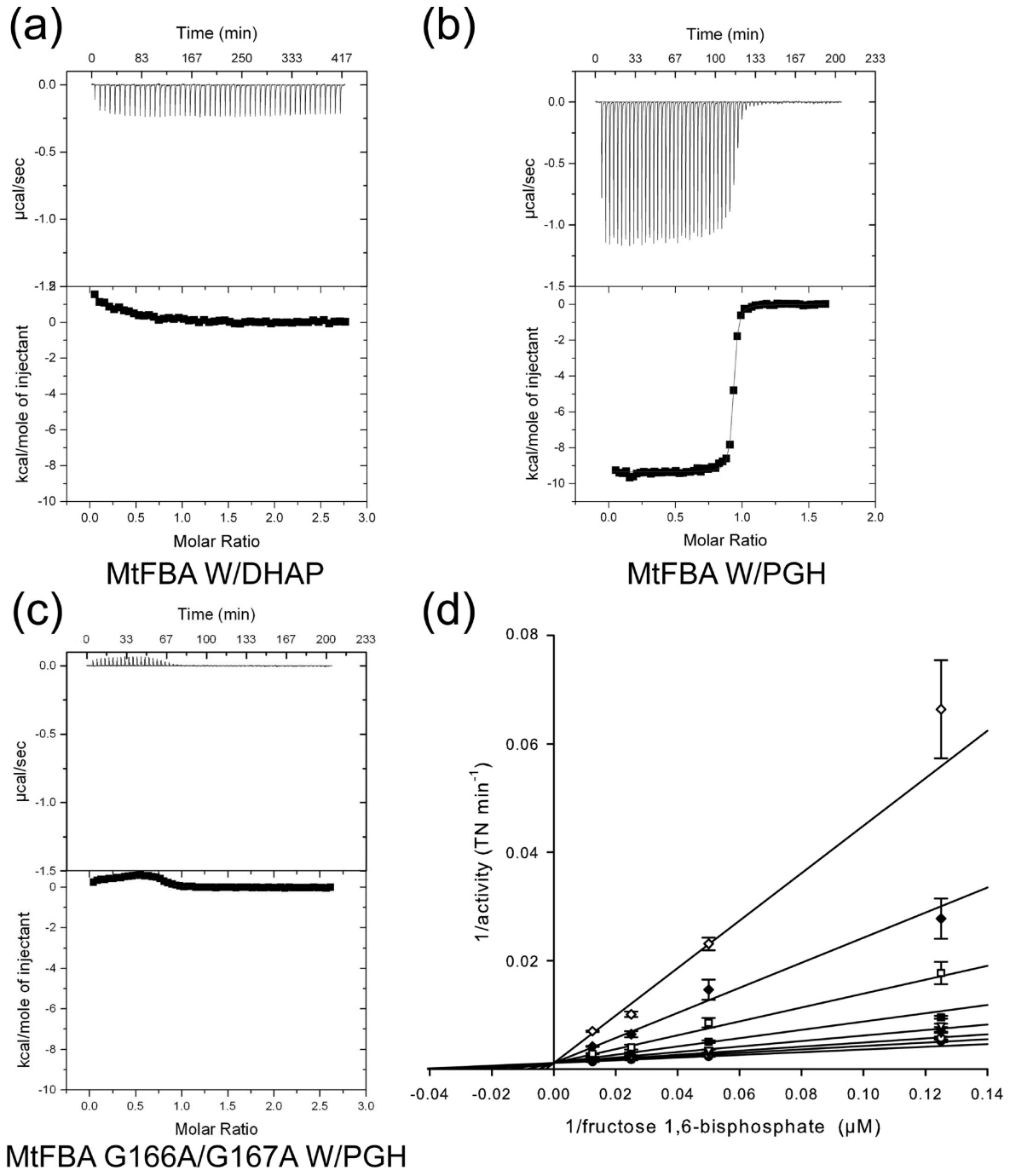

Figure 2. ITC and kinetic studies of the binding interactions of wild-type and G166A/G167A MtFBA with PGH and DHAP. ITC thermographs (top) and associated binding isotherms (bottom) of wild-type and mutant MtFBA titrated with either DHAP or PGH are shown in panels a–c. (a) Wild-type MtFBA titrated with DHAP. (b) Wild-type MtFBA titrated with PGH. Data were fit to a single-site binding model using a monomeric concentration of MtFBA (bottom). The resulting thermodynamic parameters and the value for *n* are given in the text. (c) G166A/G167A mutant MtFBA titrated with PGH. (d) Lineweaver–Burke plot of DHAP inhibition of MtFBA. DHAP concentrations were (●) 0, (○) 62.5, (▼) 125, (▽) 250, (■) 500, (□) 1000, (♦) 2000, and (◇) 4000 μM. Data were globally fit to a pure competitive inhibition model. The resulting kinetic parameters are given in the text.

μL of a 15 mg/mL MtFBA protein solution containing buffer B and 2 mM PGH (cyclohexylammonium salt) that was mixed in a 1:1 ratio with a precipitant of 26% PEG 300 and 0.1 M sodium acetate (pH 4.8). Crystals appeared within 4–5 days. MtFBA crystals without PGH were grown using the same protocol used for MtFBA–PGH crystal growth except that a 26 to 32% PEG 300 gradient was used instead. We found that the addition of 2% (w/v) DMSO as an additive caused holo-MtFBA crystals to form sporadically after 4–6 weeks.

X-ray Structural Determination of MtFBA and the MtFBA–PGH Complex. X-ray data sets for the MtFBA–PGH complex were collected at SER-CAT beamline 22-ID, while X-ray data sets for apo-MtFBA were collected at LS-CAT beamline 21-ID-D. All crystals were mounted on nylon loops and submerged in a 5 μL volume of mother liquor as a

dx.doi.org/10.1021/bi300928u | *Biochemistry* 2013, 52, 912–925

cryosolution. Crystals were subsequently flash-cooled in liquid nitrogen and mounted under a stream of dry N_2 at 100 K. All data sets were collected from a series of 0.5° rotational X-ray frames using a MAR 300 CCD detector. X-ray images were indexed, processed, integrated, and scaled together using HKL2000.[27] Because the MtFBA and MtFBA−PGH proteins crystallized in the same space group (*I*222) with unit cell dimensions similar to those of the MtFBA−substrate complexes, initial phases were readily obtained via rigid-body refinement using Refmac 6.2 and the MtFBA−DHAP [Protein Data Bank (PDB) entry 3ekl] structure without DHAP as a starting model.[2,28] WinCoot was used for model building, and Refmac 6.2 from the CCP4 suite was used for refinement.[28] Coordinates and molecular library files for the ligand PGH were generated using Sketcher in the CCP4 program suite. Isotropic temperature factors were refined, and occupancies were 1.00 for all atoms of the MtFBA−PGH and apo-MtFBA structures. Water molecules were added to $F_o - F_c$ density peaks that were greater than 3σ using the "Find Water" winCoot program function. The final models were checked for structural quality using the CCP4 suite programs Procheck and Sfcheck. The atomic coordinates and structure factors have been deposited in the Protein Data Bank (entries 4DEF and 4DEL). Simulated annealing $F_o - F_c$ and $2F_o - F_c$ density maps were generated by Phenix version 1.8.1-1168.[29]

RESULTS

Binding Affinity of PGH and DHAP for MtFBA. Because PGH has been shown to be a potent inhibitor of FBA from other species, we wanted to directly determine the dissociation constants (K_d and K_i values) for PGH and DHAP with MtFBA. Isothermal titrations of MtFBA with PGH and DHAP were performed and revealed that only the binding of PGH involves an enthalpic (ΔH) component as no heat was detected for the interaction between MtFBA and DHAP (Figure 2a,b). The resulting thermodynamic constants for the interaction of PGH per MtFBA monomer are as follows: $\Delta H = -9354 \pm 8$ cal/mol, $\Delta S = 3.75 \pm 0.02$ cal mol^{-1} K^{-1}, and $K_d = 21.1 \pm 0.2$ nM with $n = 0.90 \pm 0.04$, for PGH (Figure 2b). The absence of an enthalpic contribution to DHAP binding suggested that an additional interaction might be stabilized by PGH beyond those interactions found between DHAP and MtFBA. The similarities between the chemical structure of DHAP and PGH, along with the recently revealed MtFBA−DHAP/HEI structure, suggested that the stabilization of the active site loop might be the source of the heat observed (Figure 2b). To explore the potential link between the active site loop and the heat observed, we performed ITC on a loop stabilizing the MtFBA double mutant, G166A/G167A (Figure 2c). Although this mutant still possesses all its catalytic residues, no heat was detected for the interaction of G166A/G167A with PGH, supporting the divergent relationship between PGH and DHAP with regard to the residues with which these molecules interact in the active site loop.

Because we could not determine directly the K_d value for the binding of DHAP to MtFBA, we focused on determining the relative affinity of DHAP for MtFBA by measuring its inhibition constant (K_i) against FBP in the forward reaction. We utilized a modified version of the absorbance-based enzymatic assay that was previously used for GlFBA kinetic characterization.[21] This assay utilizes glyceraldehyde 3-phosphate dehydrogenase (GAPDH) to couple MtFBA-generated G3P to the reduction of NAD^+ to NADH. Additionally, the coupling enzyme TIM was removed from the assay to prevent the conversion of DHAP to G3P. Four different fructose 1,6-bisphosphate concentrations and five different DHAP concentrations were utilized to determine the kinetic response of MtFBA to varying concentrations of substrate and the product inhibitor DHAP. The results of the kinetic studies are shown in Figure 2d as a Lineweaver−Burk plot. The pattern in the data indicates that DHAP behaves as a competitive product inhibitor against the substrate fructose 1,6-bisphosphate with a K_i value of 238 ± 20 μM for MtFBA. This mode of inhibition is consistent with the product G3P leaving first followed by DHAP in a uni-bi kinetic scheme. This mechanism of product release also supports our previous X-ray structural data for the MtFBA−DHAP complex where we observe DHAP binding deep within the enzyme's active site pocket preventing FBP from accessing the active site zinc and catalytic relevant residues.[2] These results indicate that PGH binds to MtFBA approximately 11000 times more tightly than DHAP.

X-ray Structure of the MtFBA−PGH Complex. The observation that PGH binds to MtFBA approximately 10^4 times stronger than DHAP with a strong enthalpic contribution to binding and the observed absence of heat involved in the interaction with DHAP suggest that significantly different structural interactions must exist between the MtFBA−DHAP and MtFBA−PGH complexes. Therefore, we cocrystallized MtFBA with the inhibitor PGH, Zn^{2+}, and Na^+ under conditions similar to those used to obtain crystals of the MtFBA−DHAP complex and determined its structure to 1.58 Å resolution (Table 1).[2]

Analysis of the conformation of the biologically relevant tetramer within the unit cell revealed that the overall conformation of the enzyme and crystal packing geometry are essentially the same as those observed previously for the X-ray structures of MtFBA bound with DHAP, DHAP-G3P, or FBP,[2] or the apo-MtFBA structure.[9] Specifically, the MtFBA−PGH complex maintains a typical β/α-barrel structure composed of an eight-β-sheet core (β1−β8) surrounded by eight α-helices [α1−α8a (Figure 3a)].[2] Strikingly, well-ordered electron density within the active site was also observed for the previously elusive active site loop [residues 168−179 (Figure 3b)]. This loop region is disordered in the X-ray structures of MtFBA bound with DHAP, DHAP-G3P, or FBP.[2] However, in the MtFBA−PGH complex, additional secondary structural elements are formed, including a new β-strand (β5b) that forms an antiparallel β-sheet with residues 166−169 (β5a) and a new 3_{10}-helix (3_{10}a) that completes the formation of the active site loop (Figure 3c,d).

In addition to the newly resolved active site loop, electron density for a molecule of PGH, the active site metal cations (Zn^{2+} and Na^+), a zinc atom, an acetate molecule, and a molecule of PEG 300 are also observed in the asymmetric unit (Figure S2 of the Supporting Information). The well-resolved acetate and PEG 300 molecules are both observed within a binding pocket that is distal to the active site of the enzyme. Within this pocket, there are several polar residues, including two lysine residues, that can facilitate the binding of these ligands. The location of this pocket and the presence of these lysines may be of significance in the interaction of human plasminogen with MtFBA that was recently suggested by de la Paz Santangelo et al. They reported that interactions between plasminogen and MtFBA are dependent on MtFBA lysines and independent of the MtFBA active site.[9] Because this pocket is the only sizable cleft outside of the active site, contains lysines,

Table 1. Data Collection and Refinement Statistics

	MtFBA−PGH	apo-MtFBA
Data Collection		
space group	*I*222	*I*222
unit cell dimensions		
a, *b*, *c* (Å)	61.8, 119.6, 164.0	60.7, 119.7, 164.8
$\alpha = \beta = \gamma$ (deg)	90	90
resolution (Å)	93.90−1.58	96.9−1.64
no. of reflections observed	354909	158675
no. of unique reflections	78320	65340
R_{merge} (%)[b]	5.9 (27.9)[a]	4.5 (20.0)[a]
$I/\sigma I$	22.6 (4.2)[a]	15.7 (4.4)[a]
completeness (%)	94.0 (77.5)[a]	88.6 (94.8)[a]
Refinement		
resolution range (Å)	93.90−1.58	96.9−1.64
no. of reflections in the working set	74297	62029
no. of reflections in the test set	3910	3306
R_{work} (%)[c]	18.8	18.9
R_{free} (%)[c]	20.5	19.9
root-mean-square deviation		
bond lengths (Å)	0.01	0.01
bond angles (deg)	1.2	1.1
no. of protein/water atoms	2738/580	2444/424
average *B* factor (Å^2)		
total	24.0	29.4
protein	18.4	27.0
water	40.4	43.6
ligands	24.0	46.3
ions	20.0	39.7

[a]Data for the last resolution shell are given in parentheses. [b]$R_{merge} = \sum_h \sum_i |I_i(h) - \langle I(h)\rangle| / \sum_h \sum_i I_i(h)$, where $I_i(h)$ is the *i*th measurement and $\langle I(h)\rangle$ is the weighted mean of all measurements of $I(h)$. [c]R_{work} and $R_{free} = h[|F(h)_{obs}| - |F(h)_{calc}|]/h|F(h)_{obs}|$ for reflections in the working and test sets, respectively.

and binds ligands, this pocket might be a candidate for these MtFBA−plasminogen interactions.

MtFBA Active Site Loop. The main chain density for the previously unresolved amino acids, 168−179, of MtFBA was readily observed from $F_o - F_c$ electron density maps calculated after initial refinement (Figure S1a of the Supporting Information). When the missing backbone atoms of the loop residues were built into the electron density, the majority of the side chain residues became immediately apparent (Figure 3b). Simulated annealing electron maps also revealed density for all residues of the loop except for the expectedly flexible Gly171 located at the tip of the loop (Figure S1b,c of the Supporting Information). Formation of salt bridges between E168 and D170 and between K309 and R314 is observed, suggesting that these interactions are important in anchoring β-strand β5 within the β-turn. These two interactions also result in lower *B* factor values (<40 Å^2) for these residues, which helps produce complete side chain density for residues within β-strand β5a and the β-turn. In contrast, β-strand β5b is held in place through only one, main chain β-sheet interaction, which results in significantly higher *B* factors (40−90 Å^2) and less defined density for associated side chains (Figure 3b). The bound position of the active site loop forms a flap over the PGH-bound active site, which is distal to any dimer−dimer or intratetrameric interfaces. This orientation suggests that only intramonomer and intradimer interactions are responsible for the stabilization of the loop in its closed form (Figure 3b and Figure S2 of the Supporting Information).

PGH-Bound Active Site of MtFBA. A closer examination within the active site of the MtFBA−PGH structure reveals well-ordered electron density for PGH (Figure 4a). The hydroxyl group of PGH produces an oxygen−ZN1 bond length of <2.2 Å, which is indicative of a first-coordination sphere bond with ZN1 (Figure 4b−d). The ketone oxygen (O−C in Figure 4b) of PGH forms a longer bond with ZN1, suggesting a near first-sphere H-bond interaction. As a result, ZN1 has a distorted trigonal bipyramidal coordination geometry that is similar to the coordination geometry surrounding the active site zinc atom in the MtFBA−DHAP structure (Figure 4b).[2,30]

Although the interactions between MtFBA and PGH appear at first to be similar to those with the reaction intermediate, HEI, the newly observed and ordered conformation of the active site loop reveals additional interactions between MtFBA and PGH. These interactions are mediated through a newly observed active site water molecule, W57. This water molecule forms a 2.9 Å hydrogen bond with the hydroxamate nitrogen atom of PGH and is coordinated to D276 and E169 through hydrogen bonds. D276 has been previously implicated in the stereoselectivity of MtFBA for fructose 1,6-bisphosphate enantiomers, and E169 is located within the active site loop (Figure 4c). The orientation of the E169 side chain and its coordination to a water molecule in a position to contribute to catalysis suggest that E169 is a catalytically relevant residue likely acting through a proton shuttle mechanism.

X-ray Structure of Substrate- and Product-Free MtFBA. To probe how the binding of substrates and products influences the conformation of the active site loop and its interaction with the active site and to rule out the possibility that DHAP could have copurified with MtFBA and contributed to the observed loop density in the active site, MtFBA was crystallized in the absence of PGH or any other added MtFBA substrate or product. Crystals of the substrate-free and product-free form of the enzyme (holo-MtFBA) were grown using the same crystallization conditions that produced MtFBA−PGH crystals except that 2% DMSO was used as an additive. X-ray data were collected, and the final data processing and statistics are summarized in Table 1. Inspection of the MtFBA active site in the absence of added substrates and products or an inhibitor reveals that no ligands are bound except for an acetate molecule from the mother liquor that coordinates to the active site sodium cation (Figure 5a). Additionally, well-ordered electron density for two water molecules that occupy the first coordination sphere of the active site zinc cation (ZN1) is also observed (Figure 5). The coordination geometry surrounding the zinc atom in the active site of the holo-MtFBA enzyme is analogous to that of the EcFBA structure that was also determined in the absence of substrates and products (Figure 5a−c).[19] The presence of the zinc in the active site also correlates with the observation of zinc in the active site of MtFBA reported by Labbé et al., who used biochemical approaches.[31]

Interestingly, the active site zinc cation coordinating to the imidazole nitrogen of H212 was not observed in the active site of an MtFBA structure (MtFBA-NZ, PDB entry 4A21) that was recently determined to 2.3 Å.[9] This lower-resolution structure was determined from crystals that were grown from crystallization conditions significantly different than those used here to determine the zinc and sodium cation-bound form of MtFBA (Figure 5d).[9] The crystallization and

dx.doi.org/10.1021/bi300928u | *Biochemistry* 2013, 52, 912−925

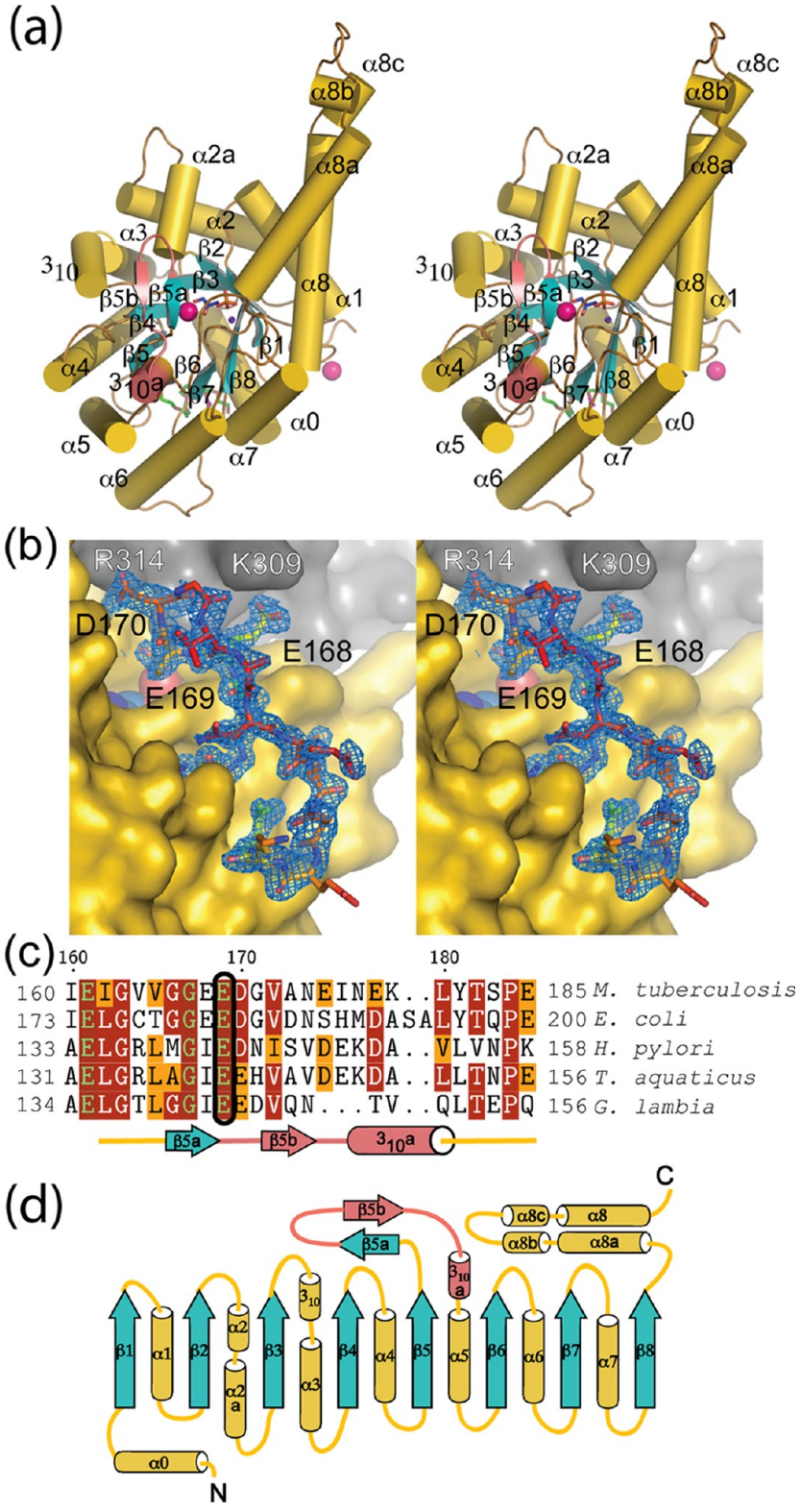

Figure 3. X-ray structure of MtFBA in complex with PGH highlighting the newly resolved active site loop. (a) Divergent-eyed stereoview of a cartoon rendering of the MtFBA–PGH protomer. Helical regions are presented as cylinders with β-strands as arrows. Helices and loops are colored yellow with strands colored light blue. Zinc ions (hot pink) are space-fill-rendered according to atomic radii with the active site sodium ion removed for the sake of clarity of PGH (blue) bound. Other ligands observed, PEG300 (green) and acetate (lavender), are present as sticks. Active site loop residues 168–179 are colored pink. (b) Divergent-eyed stereoview of the MtFBA active site loop. MtFBA residues 165–180 are rendered as sticks. Residues shown as sticks are colored according to *B* factors, with blue representing a *B* factor of ~25 Å^2 and red representing a *B* factor of ~90 Å^2. PGH is depicted in CPK with carbons colored cyan. All other residues are represented as a surface rendering with the asymmetric protomer colored yellow and the symmetry-related surface colored gray. Blue mesh reflects $2F_o - F_c$ density maps calculated for the active site loop and contoured at 1σ. (c) Sequence alignment of the active site loop region of class IIa-b FBP aldolase from the H37RV strain of *M. tuberculosis* (NP_334786), *E. coli* (PDB entry 1B57_A), *H. pylori* (PDB entry 3C4U), *T. aquaticus* (PDB entry 1RV8_A), and *G. lamblia* (PDB entry 2ISV_A). The alignment was

dx.doi.org/10.1021/bi300928u | *Biochemistry* 2013, 52, 912–925

Figure 3. continued

generated using CLUSTALW, TEXSHADE, and BL2SEQ (http://workbench.sdsc.edu/) with the following: matrix = BLOSUM62, gap opening penalty = 11, gap extension penalty = 1, and λ ratio = 0.85. Amino acids are color-coded with respect to being nonconserved (white), similar (orange), conserved (red), and completely conserved (red; green lettering) across the six sequences. Active site catalytically relevant glutamates are circled. (d) Complete secondary structure topology of MtFBA. Secondary elements are colored as in panel a.

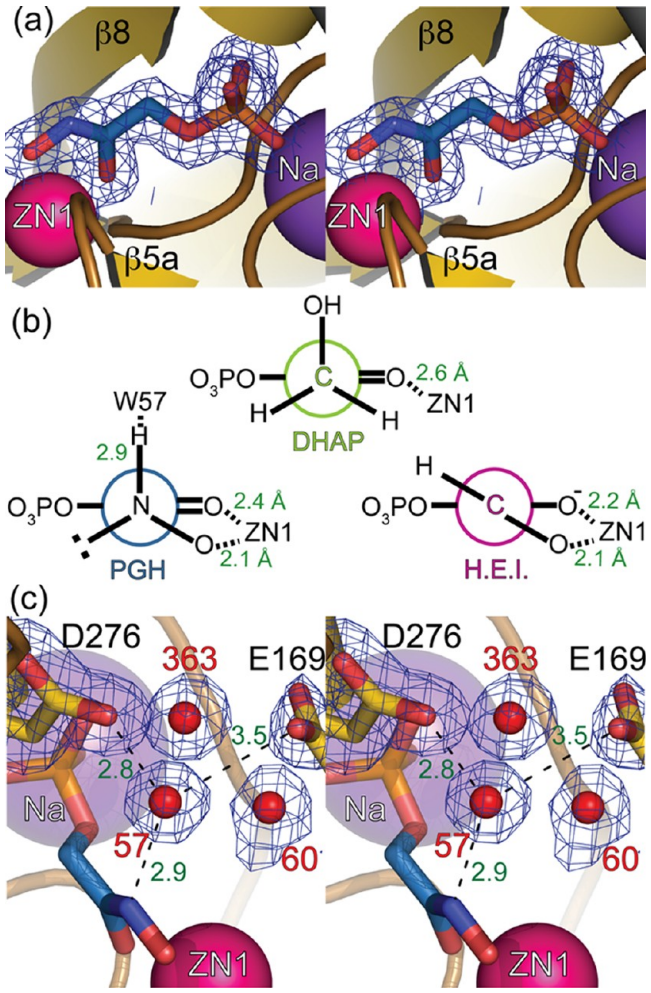

Figure 4. Structure of the MtFBA active site bound to PGH. (a) Divergent-eyed stereoview of the MtFBA active site bound to PGH (blue). The carbon atoms of the single protomer within the asymmetric unit are colored yellow. Heteroatoms are colored according to their element. Zinc (hot pink) and sodium (purple) ions are rendered as spheres according to their atomic size. The blue mesh represents the $2F_o - F_c$ electron density maps surrounding the PGH molecule. The map is contoured to 1σ. (b) Newman projection of DHAP, HEI, and PGH bound to a zinc cation (SN1) within the MtFBA active site. DHAP and HEI are from PDB entry 3KEL, and PGH is from PDB entry 4DEL. Intermolecular distances between the atoms of the bound ligands and ZN1 are colored green. These illustrate the tetrahedral molecular geometry of PGH's nitrogen, which is divergent from HEI's trigonal planar geometry. (c) Divergent-eyed stereo alternate angle view of the MtFBA active site with PGH bound. Labels of residues of the MtFBA–PGH complex are colored black, with labels for waters colored red. All other atoms are rendered as in panels a and b. H-Bond distances among W57, PGH, and MtFBA active site residues are colored green.

purification of MtFBA-NZ reported by de la Paz Santangelo et al. were achieved at high inhibitory concentrations of ammonium sulfate and lithium sulfate and in the absence of Zn^{2+}, which directly impacted the structure within the MtFBA active site.[9] Specifically, these conditions resulted in the binding of sulfate polyanions and an additional cation, presumably a sodium ion, which are bound in noncatalytically relevant positions. The identity of the additional cation (sodium, lithium, or ammonium) was not independently confirmed.[9] As a result, the X-ray structure of the substrate- and product-free form of MtFBA reported here may better represent the holoenzyme, or near apoenzyme, form of MtFBA.

Probing the Catalytic Roles of Residues within the MtFBA Active Site Loop. The well-ordered structure of the active site loop in the MtFBA–PGH complex and the available kinetic information about the EcFBA loop mutant enzymes reported by Berry and colleagues allowed us to propose possible catalytic roles for some of the same amino acids within this loop.[22] Therefore, we used site-directed mutagenesis to test whether E169 and E168 participate in the deprotonation–protonation reaction and whether the flexibility of the two glycine residues (G166 and G167) at the beginning of the loop influences the catalytic efficiency of MtFBA. In addition, we also characterized further the role of D276 in solvent exchange in the deprotonation–protonation reaction.[2,17,32,33]

The steady-state kinetic parameters and deuterium solvent isotope effects on five MtFBA mutants were determined, and the results are summarized in Table 2. The rate of FBP catalysis by MtFBA was measured using an NADH-coupled assay at room temperature, and the maximal turnover number, k_{cat}, was determined to be 720 ± 10 min^{-1} for the wild-type enzyme. This k_{cat} value is ~60% of the value reported for MtFBA by Ramsaywak et al. determined at 28 °C and ~50% of the value reported for MtFBA by Labbé et al. determined at 30 °C.[4,31] The corresponding increases in k_{cat} for MtFBA in response to increasing temperatures has also been reported by Rukseree et al., providing a basis for the differences in k_{cat} between this study and others.[4,24,31] Beyond comparisons of k_{cat} determined for MtFBA from different studies, the k_{cat} value for MtFBA determined here is comparable to the value determined for EcFBA at 30 °C.[22] It is also approximately 3 times the k_{cat} value reported for GlFBA taken at a similar temperature.[17,21] The K_m value for the interaction of FBP with MtFBA was determined to be 40 ± 1 μM and is consistent with the value for MtFBA determined previously.[4] However, the K_m value for MtFBA is 1 order of magnitude lower than that for the EcFBA enzyme and 1 order of magnitude greater than the K_m value for the GlFBA enzyme.[17,21,22]

Many class II FBAs, including MtFBA, contain two glutamate residues in tandem within the active site loop, MtFBA E168 and E169 (Figure 3c). In the case of GlFBA and TaFBA, these two glutamates are offset from those of EcFBA, which has previously been proposed to be the residue responsible for protonation and/or deprotonation of DHAP in the FBP cleavage reaction catalyzed by EcFBA.[22] Mutation of E169 to an alanine in MtFBA resulted in significant decreases in both k_{cat} (~1800-fold) and k_{cat}/K_m (~1000-fold) for the FBP cleavage reaction, whereas mutation of nearby E168 to alanine resulted in only an approximate 5-fold decrease in k_{cat} versus

dx.doi.org/10.1021/bi300928u | *Biochemistry* 2013, 52, 912–925

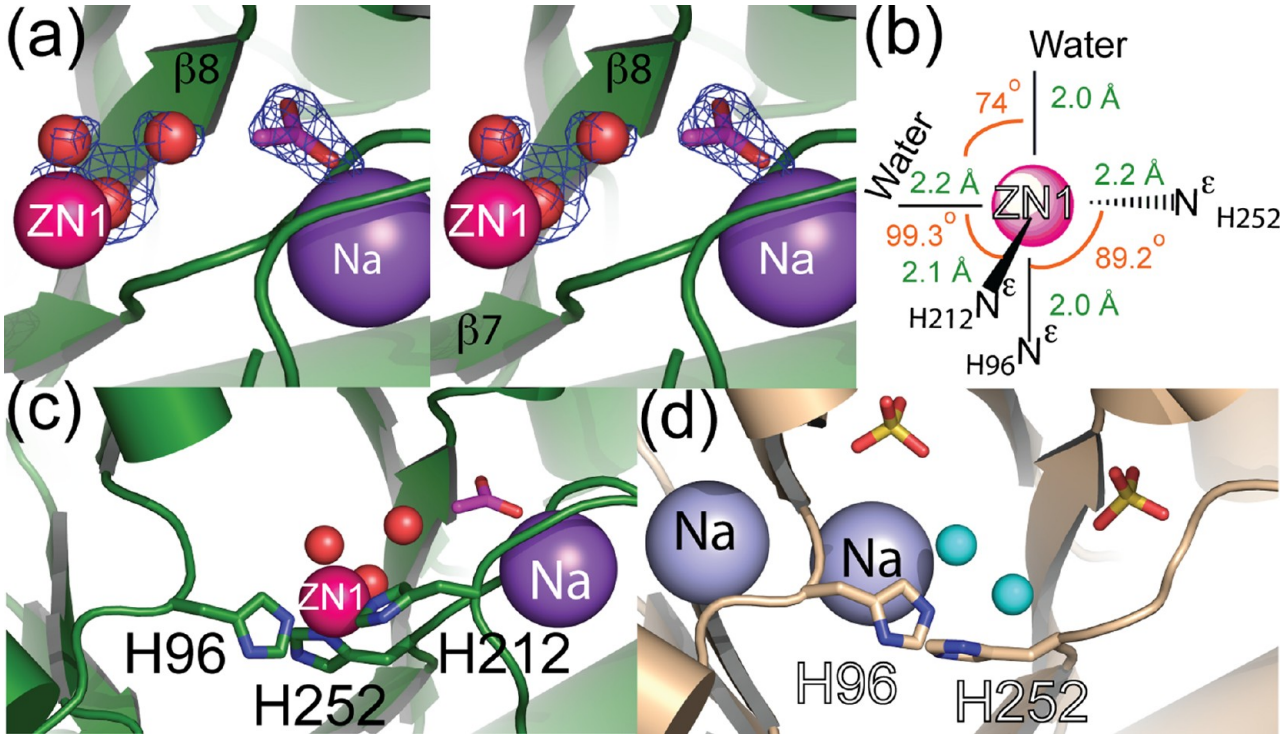

Figure 5. Active site structure of the holo-MtFBA enzyme. (a) Divergent-eyed stereoview of the apo-MtFBA active site. Asymmetric unit protomer carbons are green heteroatoms colored according to their element. Zinc (hot pink) and sodium (purple) ions are rendered as spheres according to their atomic size. Waters (red) are depicted as spheres scaled to 50% for the sake of clarity. Electron density, $2F_o - F_c$ map (blue) calculated at 1σ around waters and acetate (lavender) located within the active site. (b) Coordination schematic of ZN1 in apo-MtFBA. Distances are shown in green and angles in orange. (c) Apo-MtFBA active site. All atoms illustrated as in panel a. The acetate ion (magenta) is rendered as sticks. (d) MtFBA with no active site zinc bound (PDB entry 4A21). Sodium (lavender) ions are rendered as spheres according to their atomic size. Waters (cyan) are depicted as spheres scaled to 50% for the sake of clarity, with sulfate anions rendered as sticks.

that of wild-type MtFBA. These decreases support the MtFBA–PGH structure's assertion that E169 of MtFBA directly participates in the acid/base catalytic machinery associated with the active site loop. Also, these reductions in activity are significantly more profound than those observed for the EcFBA enzyme, ~315-fold for k_{cat} and ~600-fold for k_{cat}/K_m, suggesting that E169 may be slightly more rate-limiting in the MtFBA-catalyzed cleavage of FBP.

Additionally, a direct interaction between the carboxylate side chain of E169 and a water molecule [W57 (Figure 4c)] that is directly hydrogen bonded to the hydroxamate nitrogen of PGH is clearly observed, suggesting E169 serves as a proton shuttle that abstracts the C1 proton from DHAP (Figure 1a). In addition to the coordination of the active site water by the carboxylic side chain of E169, the carboxylic group of D276 also directly coordinates this water molecule. As observed in the MtFBA–FBP structure, D276 is expected to contribute to the binding of and stereoselectivity for FBP. Therefore, it is not surprising that the alanine mutant, D276A, elevated the K_m 5-fold.[2,17] Intriguingly, the D276A mutation also resulted in a 26-fold reduction in k_{cat}. This reduction in activity, along with the MtFBA–PGH evidence that D276 coordinates with an active site water molecule, suggests that D276's role goes beyond facilitating the binding of FBP.

We also probed the sensitivity of the FBP cleavage reaction to solvent-derived deuterons by performing deuterium solvent isotope effects. For the wild-type MtFBA enzyme, a normal solvent isotope effect on ^{D}V (k_{cat}^{H}/k_{cat}^{D} = 1.9) is observed, whereas no solvent isotope effect is observed on $^{D}(V/K)$ [$(k_{cat}/K_m)^{H}/(k_{cat}/K_m)^{D}$ = 0.94], suggesting proton transfer is partially rate-limiting in the ES complex (Table 2c). In contrast, normal solvent isotope effects are observed on both ^{D}V (k_{cat}^{H}/k_{cat}^{D} = 2.1) and $^{D}(V/K)$ [$(k_{cat}/K_m)^{H}/(k_{cat}/K_m)^{D}$ = 2.5] for E169A MtFBA. Also, significant solvent isotope effects are observed for single and double MtFBA loop mutants, $^{D}(V/K)$s [$(k_{cat}/K_m)^{H}/(k_{cat}/K_m)^{D}$ = 3.2 and 3.5, respectively].

DISCUSSION

Roles of Key Active Site Loop Residues of MtFBA. Previously, the inability to visualize the MtFBA active site loop left ambiguity as to which residues within this loop participate in the catalytic mechanism of MtFBA. Mutagenesis studies and primary kinetic isotope effects on the deprotonation of [1(*S*)-^{2}H]DHAP by Berry and co-workers conducted with EcFBA implicated residue E182 within the active site loop of EcFBA as being directly involved in the protonation–deprotonation step of the FBA-mediated reaction.[22] However, direct structural proof of the interaction of E182 with substrates, intermediates, or products could not be achieved as the active site loop was always disordered in X-ray structures. As in EcFBA, TaFBA, and GlFBA, MtFBA has two tandem glutamates, E168 and E169, within the active site loop. Furthermore, whether the glutamate directly acted on substrates of MtFBA or exerted its function through a water molecule was previously unclear. The MtFBA–PGH structure reported here provides insight into both these issues. Visualization of E169 within the MtFBA active site is experimentally clear, and the side chain of E169 coordinates a water molecule that is H-bonded to PGH. This observation clearly advocates E169 as the glutamate involved in protonation

dx.doi.org/10.1021/bi300928u | *Biochemistry* 2013, 52, 912–925

Table 2. Kinetic Parameters for MtFBA

(a) Fructose 1,6-Bisphosphate (H_2O)[a]			
enzyme	k_{cat}[c] (min^{-1})	K_m (μM)	k_{cat}/K_m[d] (μM^{-1} min^{-1})
wild-type	720 ± 10	40 ± 1	18 ± 1
E169A	0.40 ± 0.04	18 ± 1	0.017 ± 0.002
E168A	160 ± 10	30 ± 2	5.3 ± 0.5
G167A	10 ± 1	21 ± 1	0.48 ± 0.05
G167A/G166A	6.6 ± 0.1	21 ± 2	0.32 ± 0.03
D276A	27 ± 1	180 ± 10	0.15 ± 0.01
(b) Fructose 1,6-Bisphosphate (D_2O)[b]			
enzyme	k_{cat} (min^{-1})	K_m (μM)	k_{cat}/K_m (μM^{-1} min^{-1})
wild-type	370 ± 10	19 ± 1	19 ± 1
E169A	0.16 ± 0.01	14 ± 1	0.011 ± 0.001
E168A	50 ± 0.5	5.9 ± 0.5	8.7 ± 0.7
G167A	3.0 ± 0.1	20 ± 1	0.15 ± 0.01
G167A/G166A	1.9 ± 0.1	13 ± 1	0.15 ± 0.01
D276A	34 ± 1	180 ± 10	0.19 ± 0.01
(c) Isotope Effect Relationships			
enzyme	k_{cat}^H/k_{cat}^D	K_m^H/K_m^D	$(k_{cat}/K_m)^H/(k_{cat}/K_m)^D$
wild-type	1.9 ± 0.1	2.1 ± 0.2	0.94 ± 0.07
E169A	2.5 ± 0.3	1.3 ± 0.2	2.0 ± 0.3
E168A	3.2 ± 0.2	5.1 ± 0.5	0.61 ± 0.07
G167A	3.2 ± 0.4	1.1 ± 0.1	3.20 ± 0.4
G167A/G166A	3.5 ± 0.2	1.6 ± 0.16	2.13 ± 0.24
D276A	0.80 ± 0.03	1.02 ± 0.06	0.79 ± 0.06

[a]The steady-state kinetic parameters were determined in 100 mM Tris-HCl, 100 mM potassium acetate, and 0.4 mM NADH (pH 7.4) at 24 °C. [b]The steady-state kinetic parameters were determined in 100 mM-Tris HCl, 100 mM potassium acetate, and 0.4 mM NADH (pH 7.8/pD 7.4) at 24 °C. [c]Errors for k_{cat} and K_m are from the fit. [d]Errors for k_{cat}/K_m and those for $(k_{cat}/K_m)^H/(k_{cat}/K_m)^D$ were calculated using $D(A/B) = (A/B)[(DA/A)^2 + (DB/B)^2]^{1/2}$, where DA and DB represent the errors in A and B, respectively.

and/or deprotonation in MtFBA and that it functions through a proton shuttle mechanism with a water molecule. Because this glutamate aligns with E182 of EcFBA upon sequence comparison, and its mutation to alanine resulted in the most catalytically hindered mutation between the two glutamates (Table 2a), these results corroborate the assignment by Berry and colleagues that E182 in EcFBA functions as the catalytic acid/base. Finally, the solvent isotope effects observed for the selected MtFBA mutants support the importance of E169 in the catalytic mechanism.

For an enzyme to exhibit a solvent isotope effect, the rate-limiting step must involve the breakage or formation of bonds that involve solvent-derived deuterons. For class II FBAs, this translates to the protonation−deprotonation steps.[22] Of the wild type and five mutant FBAs evaluated, only the E169A and MtFBA loop mutations that likely restrict E169 to be positioned in a catalytically relevant position or that prevent E169 from being in the active site at all exhibited a significant isotope effect $[(k_{cat}/K_m)^H/(k_{cat}/K_m)^D > 1$ (Table 2)]. With no isotope effect observed for E168A, and a significant effect on k_{cat} for the E169A mutation, the identity of E169 as the residue responsible for protonation and/or deprotonation in MtFBA is revealed and protonation facilitated by E169 during FBP cleavage becomes more rate-limiting in the E169A mutant. Unfortunately, these results could not be compared in total with those compiled for EcFBA, as that study did not include an equivalent E168A mutant. However, these results do complement those obtained from EcFBA.

For EcFBA, primary isotope effects were measured for the reverse reaction with [1(*S*)-^{2}H]DHAP as the substrate, whereas we determined the solvent isotope effect of FBP cleavage by MtFBA. The mechanism of MtFBA suggests that up to five enzyme states may exist (Figure 1a). These five enzymes states comprise one for the holoenzyme as well as four others representing the different states of the ES and EP complexes (Figure 1b). Intriguingly, at least three steps, 2, 4, and 5 (Figure 1b), are potentially sensitive to solvent isotope effects. Naturally, when glutamate is mutated to alanine, the mechanistic steps that utilize this residue will become more rate-limiting (Table 2c). Interestingly, as in the EcFBA primary isotope study, no solvent isotope effect on $^D(V/K_m)$ for wild-type MtFBA was observed, suggesting that either the active site loop protonation or deprotonation is not the rate-limiting step or the isotope effect on this step is masked by increases in the energy barriers of other solvent isotope sensitive steps (Figure 1b). A value of 1.93 for ^DV with wild-type MtFBA supports the latter explanation and suggests that the proton-transferring step facilitated by the side chain of E169 is partially rate-limiting.

Mechanism of MtFBA Inhibition by PGH. Because DHAP was found to be a competitive inhibitor against FBP for MtFBA, the K_i value derived from the kinetic studies is therefore a dissociation constant for DHAP from the MtFBA−DHAP complex. Comparison of the K_d values for the DHAP−MtFBA and PGH−MtFBA complexes reveals an 11333-fold increase in affinity of PGH over DHAP for MtFBA. The MtFBA−PGH structure and accompanying results of ITC and kinetic experiments support a possible mechanism for the increase in affinity. Unlike the extra density observed in the MtFBA−DHAP structure, which was ascribed to the presence of DHAP in addition to that of the HEI intermediate, no such density is observed in the MtFBA−PGH active site (Figure 4a). This reinforces the assignment of PGH in the active site of the MtFBA−PGH complex and the assertion that HEI is observed in the MtFBA−DHAP active site.[2] In contrast to C1 of HEI that forms an sp^2 hybridized orbital system in its coordination with ZN1, a geometry suggested by its 118° bond angle, and the oxygen−zinc distances resembling two coordinating bonds, PGH adopts a tetrahedral sp^3 geometry with an angle of ∼109° among PGH's nitrogen, its bound oxygen, and the hydrogen-bonded active site water (Figure 4c). Additionally, only the nitrogen-bound oxygen of PGH forms a coordinating bond with the catalytic zinc, whereas its carbon bound oxygen's bond with the catalytic zinc resembles a longer H-bond. This suggests that the PGH's carbon-bound oxygen is in a ketone form. This narrows the possible resonance species of PGH found within the MtFBA active site to two forms, **2** or **6**, in Figure 6a. Although the distance between the PGH hydroxyl oxygen atom and ZN1 favors the assignment of species **2** to PGH within the active site, the low pH of the crystallization solution would likely favor the protonated form of **2**, which is species **6** (Figure 5b).[34] In either case, the interatomic distances among PGH, W57, E169, and D276, as well as the tetrahedral geometry of the secondary amine, which includes the lone electron pair, suggest the formation of an H-bond network as depicted in Figure 6b. In this scheme, a lone pair of electrons on the secondary amine points toward the back of the MtFBA active site, while W57 forms H-bonds with D276 and E169. This facilitates W57's involvement in extracting a proton from PGH. However, as reflected in the types of bonds formed between ZN1 and PGH as well as PGH's electron configuration, the secondary amine is not polarized to allow proton extraction as

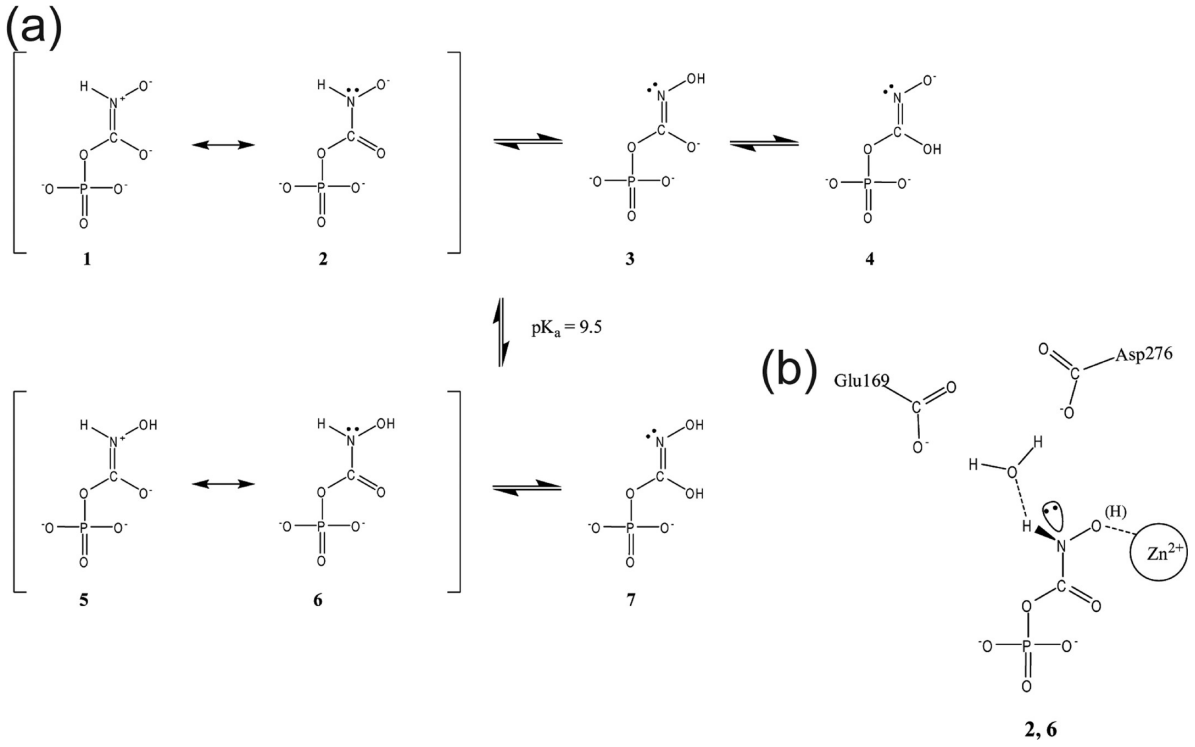

Figure 6. Ionization and tautomeric forms of PGH in solution or in the MtFBA active site. (a) Plausible forms of PGH in solution under various pH conditions.[35] (b) Coordination of PGH within the MtFBA active site.

occurs with the hydroxymethylene hydrogen atoms of DHAP.[2,5] Thus, the water molecule fails to strip the proton from PGH and instead forms a stable H-bond network among PGH, W57, D276, and E169. This network stabilizes the active site loop in a closed conformation, preventing PGH from being readily exchanged with MtFBA substrates likely contributing to PGH's robust inhibitory properties.

The isoelectronic similarity between DHAP and PGH suggests that they should block the same space in the MtFBA active site from FBP binding or displace the same two waters observed in the holo-MtFBA active site (Figure 5a). As a result, they both would have the same entropic component for binding. However, PGH possesses a vastly higher affinity for MtFBA than DHAP. This implies a significant disparity in enthalpic contributions of binding between the DHAP and PGH, which is in line with the significant heat associated with binding of PGH to MtFBA and the lack of heat associated with DHAP binding observed in ITC experiments (Figure 2). The heat observed from the binding of PGH suggests formation of stable bonds between MtFBA and PGH, which are not present between MtFBA and DHAP. Comparison of the MtFBA–DHAP and MtFBA–PGH structures bears this out with three antiparallel β-sheet H-bonds, two salt bridges, and a network of H-bonds among E169, a water molecule, D276, and PGH formed in the MtFBA–PGH structure, whereas no density for the active site loop is found in the MtFBA–DHAP structure.[2] As both the MtFBA–DHAP and MtFBA–PGH complexes possess the ability to form similar inter-MtFBA interactions, the interaction with E169 and PGH appears to be the discerning factor in stabilizing the active site loop in MtFBA.

Previous structural studies of class II FBAs utilized PGH to mimic HEI but were unable to elucidate the active site loop and any additional interactions that modulate loop stabilization beyond those formed directly by PGH and active site waters.[5,13,17] In the case of MtFBA, these interactions are formed by two salt bridges between D170 and E168 and between D314 and K308 (Figure 3b). As class IIb FBAs, both GlFBA and HpFBA lack the equivalent K309 of MtFBA as well as the presence of an isoleucine or aspartic acid residue inserted intohe active site loop just prior to the active loop glutamates.[13,17] As a class IIa FBA, EcFBA does have the conserved residues that could potentially form these salt ridges to stabilize the loop in a catalytically relevant orientation. However, high concentrations of zinc, 2–5 mM, were used to determine the EcFBA–PGH structure, and this may have artificially created an additional zinc-binding site near EcFBA's active site loop. This additional zinc site was not observed in the MtFBA structures elucidated in the presence of 0.1 mM zinc. The additional zinc found in EcFBA may have altered the active site of the EcFBA–PGH complex by forming a bond with E181, orienting E182 to form a salt bridge with EcFBA's R334.[5] Consequently, the active site loop of the EcFBA–PGH complex may have been prevented from adopting an orientation similar to that of the active site loop of the MtFBA–PGH complex.[2] Another possibility for being able to trap the active site loop of MtFBA with PGH bound is the pH of the crystallization solution. Whereas the MtFBA–PGH complex was crystallized under mildly acidic conditions, the EcFBA–PGH, GlFBA–PGH, and HpFBA–PGH structures were all resolved under mildly basic conditions.[5,13,17] However, the MtFBA–DHAP–HEI structure was crystallized under the same conditions that were used for crystallization of the MtFBA–PGH complex, and similar to the case for the EcFBA–PGH and GlFBA–PGH complexes, no electron density was observed for the active site loop. Additionally, a mixture of the substrate, DHAP, and the reaction intermediate, HEI, was found in the active site of MtFBA cocrystallized with an excess concentration of DHAP, suggesting that under MtFBA–PGH

dx.doi.org/10.1021/bi300928u | *Biochemistry* 2013, 52, 912–925

crystallization conditions, proton transfer can still occur.[2] Overall, these observations suggest that the presence of PGH and possibly the greater presence of protonated water within the active site of the MtFBA–PGH complex may contribute to the stability of the active site loop in a closed state.

In conclusion, through X-ray crystallographic visualization of the potent inhibitor PGH bound to the active site of the MtFBA enzyme, significant insight into the contribution of the active site loop to the catalytic mechanism of protonation and/or deprotonation in class II FBAs can now be envisioned. Additionally, key active site loop residues in MtFBA, specifically E169 and a catalytic water molecule, have been identified. As a result, an improved understanding of how class II FBAs perform this critical step in the cleavage of FBP into DHAP and G3P has been achieved. The MtFBA–PGH structure also illustrates a mechanism that explains the 3 order of magnitude increase in affinity of PGH over DHAP for the active sites of FBAs. PGH's ability to form favorable active site loop stabilizing interactions to elicit this increase in affinity underlines the importance and necessity of developing inhibitors that possess similar interactions with bacterial class II FBA active site loops.

■ ASSOCIATED CONTENT

Supporting Information

A view of the MtFBA active site loop with its associated electron density shown as an $F_o - F_c$ omit map, a $2F_o - F_c$ simulated annealing map, and an $F_o - F_c$ simulated annealing map (Figure S1) and the location of the active site loop of the MtFBA–PGH complex in relation to the MtFBA–PGH tetramer (Figure S2). This material is available free of charge via the Internet at http://pubs.acs.org.

Accession Codes

The atomic coordinates and structure factors have been deposited with the Protein Data Bank as entries 4DEF and 4DEL.

■ AUTHOR INFORMATION

Corresponding Author

*A.D.M.: Department of Biological Sciences and Purdue Center for Cancer Research, Purdue University, West Lafayette, IN 47907; telephone, (312) 996-1877; e-mail, amesecar@purdue.edu. S.D.P.: Eleanor Roosevelt Institute and Department of Chemistry and Biochemistry, University of Denver, 2190 E. Iliff Ave., Olin 202, Denver, CO 80208; telephone, (303) 871-2533; e-mail, spegan@du.edu.

Funding

This research was supported in part by grants from the National Center for Genetic Engineering and Biotechnology, Thailand (K.R.), Professional Research Opportunities for Faculty (S.D.P.), the Colorado Center for Drug Discovery (S.D.P.), and the Walther Cancer Foundation (A.D.M.).

Notes

The authors declare no competing financial interest.

■ ACKNOWLEDGMENTS

We thank the supporting member institutions of SER-CAT 22-BM and LS-CAT at the Advanced Photon Source, Argonne National Laboratory; these institutions can be found at http://www.ser-cat.org/members.html and http://ls-cat.org, respectively. X-ray data were collected at the Life Sciences Collaborative Access Team (LS-CAT) 21-ID-D beamline and the Southeast Regional Collaborative Access Team (SER-CAT) 22-ID beamline located at the Advanced Photon Source, Argonne National Laboratory. Use of the Advanced Photon Source was supported by the U.S. Department of Energy, Office of Science, Office of Basic Energy Sciences, under Contracts DE-AC02-06CH11357 and W-31-109-Eng-38. Use of LS-CAT Sector 21 was also supported by the Michigan Economic Development Corp. and the Michigan Technology Tri-Corridor for the support of this research program (Grant 085P1000817).

■ ABBREVIATIONS

BSA, bovine serum albumin; CHA, cyclohexylamine; DHAP, dihydroxyacetone phosphate; DMSO, dimethyl sulfoxide; EcFBA, *E. coli* class II fructose 1,6-bisphosphate aldolase; FBP, fructose 1,6-bisphosphate; GlFBA, *G. lamblia* class II fructose 1,6-bisphosphate aldolase; G3P, glyceraldehyde 3-phosphate; HEI, hydroxyenolate intermediate; HEPES, *N*-(2-hydroxyethyl)piperazine-*N*′-2-ethanesulfonate; HpFBA, *H. pylori* class II fructose 1,6-bisphosphate aldolase; ITC, isothermal titration calorimetry; IPTG, isopropyl β-D-thiogalactoside; LB, Luria-Bertani; MtFBA, *M. tuberculosis* class II fructose 1,6-bisphosphate aldolase; PGA, phosphoglycolamide; PGH, phosphoglycolohydroxamate; NADH, nicotinamide adenine dinucleotide; NMR, nuclear magnetic resonance; PEG, polyethylene glycol; PCR, polymerase chain reaction; SDS–PAGE, sodium dodecyl sulfate–polyacrylamide gel electrophoresis; TaFBA, *T. aquaticus* class II fructose 1,6-bisphosphate aldolase; TIM, triosephosphate isomerase.

■ REFERENCES

(1) Marsh, J. J., and Lebherz, H. G. (1992) Fructose-bisphosphate aldolases: An evolutionary history. *Trends Biochem. Sci. 17*, 110–113.

(2) Pegan, S. D., Rukseree, K., Franzblau, S. G., and Mesecar, A. D. (2009) Structural basis for catalysis of a tetrameric class IIa fructose 1,6-bisphosphate aldolase from *Mycobacterium tuberculosis*. *J. Mol. Biol. 386*, 1038–1053.

(3) Rutter, W. J. (1964) Evolution of Aldolase. *Fed. Proc. 23*, 1248–1257.

(4) Ramsaywak, P. C., Labbe, G., Siemann, S., Dmitrienko, G. I., and Guillemette, J. G. (2004) Molecular cloning, expression, purification, and characterization of fructose 1,6-bisphosphate aldolase from *Mycobacterium tuberculosis*: A novel Class II A tetramer. *Protein Expression Purif. 37*, 220–228.

(5) Hall, D. R., Leonard, G. A., Reed, C. D., Watt, C. I., Berry, A., and Hunter, W. N. (1999) The crystal structure of *Escherichia coli* class II fructose-1,6-bisphosphate aldolase in complex with phosphoglycolohydroxamate reveals details of mechanism and specificity. *J. Mol. Biol. 287*, 383–394.

(6) Gerdes, S. Y., Scholle, M. D., Campbell, J. W., Balazsi, G., Ravasz, E., Daugherty, M. D., Somera, A. L., Kyrpides, N. C., Anderson, I., Gelfand, M. S., Bhattacharya, A., Kapatral, V., D'Souza, M., Baev, M. V., Grechkin, Y., Mseeh, F., Fonstein, M. Y., Overbeek, R., Barabasi, A. L., Oltvai, Z. N., and Osterman, A. L. (2003) Experimental determination and system level analysis of essential genes in *Escherichia coli* MG1655. *J. Bacteriol. 185*, 5673–5684.

(7) Baba, T., Ara, T., Hasegawa, M., Takai, Y., Okumura, Y., Baba, M., Datsenko, K. A., Tomita, M., Wanner, B. L., and Mori, H. (2006) Construction of *Escherichia coli* K-12 in-frame, single-gene knockout mutants: The Keio collection. *Mol. Syst. Biol. 2*, 2006-0008.

(8) Wehmeier, U. F. (2001) Molecular cloning, nucleotide sequence and structural analysis of the *Streptomyces galbus* DSM40480 *fda* gene: The *S. galbus* fructose-1,6-bisphosphate aldolase is a member of the class II aldolases. *FEMS Microbiol. Lett. 197*, 53–58.

(9) de la Paz Santangelo, M., Gest, P. M., Guerin, M. E., Coincon, M., Pham, H., Ryan, G., Puckett, S. E., Spencer, J. S., Gonzalez-Juarrero,

M., Daher, R., Lenaerts, A. J., Schnappinger, D., Therisod, M., Ehrt, S., Sygusch, J., and Jackson, M. (2011) Glycolytic and non-glycolytic functions of *Mycobacterium tuberculosis* fructose-1,6-bisphosphate aldolase, an essential enzyme produced by replicating and non-replicating bacilli. *J. Biol. Chem. 286*, 40219−40231.
(10) Bai, N. J., Pai, M. R., Murthy, P. S., and Venkitasubramanian, T. A. (1974) Effect of oxygen tension on the aldolases of *Mycobacterium tuberculosis* H37Rv. *FEBS Lett. 45*, 68−70.
(11) Scamuffa, M. D., and Caprioli, R. M. (1980) Comparison of the mechanisms of two distinct aldolases from *Escherichia coli* grown on gluconeogenic substrates. *Biochim. Biophys. Acta 614*, 583−590.
(12) Rosenkrands, I., Slayden, R. A., Crawford, J., Aagaard, C., Barry, C. E., III, and Andersen, P. (2002) Hypoxic response of *Mycobacterium tuberculosis* studied by metabolic labeling and proteome analysis of cellular and extracellular proteins. *J. Bacteriol. 184*, 3485−3491.
(13) Fonvielle, M., Coincon, M., Daher, R., Desbenoit, N., Kosieradzka, K., Barilone, N., Gicquel, B., Sygusch, J., Jackson, M., and Therisod, M. (2008) Synthesis and biochemical evaluation of selective inhibitors of class II fructose bisphosphate aldolases: Towards new synthetic antibiotics. *Chemistry 14*, 8521−8529.
(14) World Health Organization (2008) *Global tuberculossis control: Surveillance, planning, financing*, pp 1−5, Geneva.
(15) World Health Organization (2008) *Tuberculosis MDR-TB & XDR-TB*, Geneva.
(16) Collins, K. D. (1974) An activated intermediate analogue. The use of phosphoglycolohydroxamate as a stable analogue of a transiently occurring dihydroxyacetone phosphate-derived enolate in enzymatic catalysis. *J. Biol. Chem. 249*, 136−142.
(17) Galkin, A., Li, Z., Li, L., Kulakova, L., Pal, L. R., Dunaway-Mariano, D., and Herzberg, O. (2009) Structural insights into the substrate binding and stereoselectivity of *Giardia* fructose-1,6-bisphosphate aldolase. *Biochemistry 48*, 3186−3196.
(18) Fonvielle, M., Weber, P., Dabkowska, K., and Therisod, M. (2004) New highly selective inhibitors of class II fructose-1,6-bisphosphate aldolases. *Bioorg. Med. Chem. Lett. 14*, 2923−2926.
(19) Cooper, S. J., Leonard, G. A., McSweeney, S. M., Thompson, A. W., Naismith, J. H., Qamar, S., Plater, A., Berry, A., and Hunter, W. N. (1996) The crystal structure of a class II fructose-1,6-bisphosphate aldolase shows a novel binuclear metal-binding active site embedded in a familiar fold. *Structure 4*, 1303−1315.
(20) Izard, T., and Sygusch, J. (2004) Induced fit movements and metal cofactor selectivity of class II aldolases: Structure of *Thermus aquaticus* fructose-1,6-bisphosphate aldolase. *J. Biol. Chem. 279*, 11825−11833.
(21) Galkin, A., Kulakova, L., Melamud, E., Li, L., Wu, C., Mariano, P., Dunaway-Mariano, D., Nash, T. E., and Herzberg, O. (2007) Characterization, kinetics, and crystal structures of fructose-1,6-bisphosphate aldolase from the human parasite, *Giardia lamblia*. *J. Biol. Chem. 282*, 4859−4867.
(22) Zgiby, S., Plater, A. R., Bates, M. A., Thomson, G. J., and Berry, A. (2002) A functional role for a flexible loop containing Glu182 in the class II fructose-1,6-bisphosphate aldolase from *Escherichia coli*. *J. Mol. Biol. 315*, 131−140.
(23) Weber, P., Fonvielle, M., and Therisod, M. (2003) New facile synthesis of phosphoglycolohydroxamic acid and other phosphoglycolic acid derivatives. *Tetrahedron Lett. 44*, 9047−9049.
(24) Rukseree, K., Thammarongtham, C., and Palittapongarnpim, P. (2008) One-step purification and characterization of a fully active histidine-tagged Class II fructose-1,6-bisphosphate aldolase from *Mycobacterium tuberculosis*. *Enzyme Microb. Technol. 43*, 500−506.
(25) Gill, S., and von Hippel, P. (1989) Calculation of protein extinction coefficients from amino acid sequence data. *Anal. Biochem. 182*, 319−326.
(26) Krezel, A., and Bal, W. (2004) A formula for correlating pKa values determined in D_2O and H_2O. *J. Inorg. Biochem. 98*, 161−166.
(27) Otwinowski, Z., and Minor, W. (1997) Processing of X-ray Diffraction Data Collected in Oscillation Mode. *Methods in Enzymology*, Vol. *276*, Macromolecular Crystallography, Part A, Academic Press, New York.
(28) Collaborative Computational Project Number 4 (1994) The CCP4 suite: Programs for protein crystallography. *Acta Crystallogr. D50*, 760−763.
(29) Adams, P. D., Afonine, P. V., Bunkoczi, G., Chen, V. B., Davis, I. W., Echols, N., Headd, J. J., Hung, L. W., Kapral, G. J., Grosse-Kunstleve, R. W., McCoy, A. J., Moriarty, N. W., Oeffner, R., Read, R. J., Richardson, D. C., Richardson, J. S., Terwilliger, T. C., and Zwart, P. H. (2010) PHENIX: A comprehensive Python-based system for macromolecular structure solution. *Acta Crystallogr. D66*, 213−221.
(30) Alberts, I. L., Nadassy, K., and Wodak, S. J. (1998) Analysis of zinc binding sites in protein crystal structures. *Protein Sci. 7*, 1700−1716.
(31) Labbe, G., de Groot, S., Rasmusson, T., Milojevic, G., Dmitrienko, G. I., and Guillemette, J. G. (2011) Evaluation of four microbial Class II fructose 1,6-bisphosphate aldolase enzymes for use as biocatalysts. *Protein Expression Purif. 80*, 224−233.
(32) Zgiby, S. M., Thomson, G. J., Qamar, S., and Berry, A. (2000) Exploring substrate binding and discrimination in fructose 1,6-bisphosphate and tagatose 1,6-bisphosphate aldolases. *Eur. J. Biochem. 267*, 1858−1868.
(33) Hall, D. R., Bond, C. S., Leonard, G. A., Watt, C. I., Berry, A., and Hunter, W. N. (2002) Structure of tagatose-1,6-bisphosphate aldolase. Insight into chiral discrimination, mechanism, and specificity of class II aldolases. *J. Biol. Chem. 277*, 22018−22024.
(34) Roos, A. K., Burgos, E., Ericsson, D. J., Salmon, L., and Mowbray, S. L. (2005) Competitive inhibitors of *Mycobacterium tuberculosis* ribose-5-phosphate isomerase B reveal new information about the reaction mechanism. *J. Biol. Chem. 280*, 6416−6422.
(35) Harris, T. K., Abeygunawardana, C., and Mildvan, A. S. (1997) NMR studies of the role of hydrogen bonding in the mechanism of triosephosphate isomerase. *Biochemistry 36*, 14661−14675.